Hyperfine Interactions (2021) 242: 27
https://doi.org/10.1007/s10751-021-01758-y

Nanostructured FeNiZrB powders synthesized by high-energy ball milling: structural and hyperfine characterizations

V. A. Peña Rodríguez[1,2] · J. Medina Medina[1] · C. Rojas-Ayala[1] · P. Paucar Cabrera[1] · C. V. Landauro[1,2] · J. Quispe-Marcatoma[1,2] · J. Rojas Tapia[1] · E. M. Baggio-Saitovitch[3] · E. C. Passamani[4]

Accepted: 27 October 2021 / Published online: 10 November 2021

Abstract

Nanostructured $(Fe_{0.5}Ni_{0.5})_{92}Zr_5B_3$ alloy was prepared by milling a blend of pre-alloyed $Fe_{50}Ni_{50}$ precursor and high purity chemical elemental powders of Zr and B in a high-energy ball mill setup. Rietveld refinement of the X-ray diffraction pattern of the final sample (30 h of milling) revealed presence of two Fe–Ni rich phases [disordered fcc γ–(Fe,Ni) alloy with Zr and B and the atomically ordered FeNi] with grain sizes in nanometer scale. Fe and Ni atoms were locally probed using extended X-ray absorption fine structure EXAFS and ^{57}Fe Mössbauer spectroscopy. Whilst EXAFS analysis of milled samples suggested structural properties similar to the pre-alloyed precursor, Mössbauer data have shown the Fe_2B phase formation after 3 h of milling, suggesting that the final material consists of nanograins of ordered FeNi (8%) and Fe_2B (6%) phases dispersed in solid solution of γ–(Fe,Ni) alloy rich in nickel (86%) with Zr and B atoms impregnated in grain boundary defects.

Keywords Nanostructured materials · High energy ball milling · Hyperfine interactions · Extended X-ray absorption fine structure · Tetrataenite

This article is part of the Topical Collection on *Proceedings of the International Conference on the Applications of the Mössbauer Effect (ICAME 2021), 5-10 September 2021, Brasov, Romania*
Edited by Victor Kuncser

✉ V. A. Peña Rodríguez
vpenar@unmsm.edu.pe

✉ J. Medina Medina
jose.medina@unmsm.edu.pe

[1] Facultad de Ciencias Físicas, Universidad Nacional Mayor de San Marcos, P.O. Box 14-0149, Lima 14, Peru

[2] Centro de Investigaciones Tecnológicas, Biomédicas y Medioambientales, Ca. José Santos Chocano 199, Ciudad Universitaria, Bellavista Callao, Peru

[3] Centro Brasileiro de Pesquisas Físicas, Rua. Dr. Xavier Sigaud 150, Urca, Rio de Janeiro CEP 22290-180, Brazil

[4] Departamento de Física, Universidade Federal do Espírito Santo, Vitória, ES 29075-910, Brazil

1 Introduction

Since 70´s, several experimental procedures have extensively been developed and applied to produce nanostructured and amorphous materials [1–10]. For instance, the mechanical alloying (MA) process was originally applied to prepare oxide-dispersion strengthened nickel- and iron-based super-alloys [1, 2]. It becomes now one of the most powerful methods for material processing in powder form, because of a broad variety of equilibrium (intermetallic compounds) and non-equilibrium phases (amorphous, nanocrystalline, quasicrystalline, and supersaturated solid solutions [2–4]) that can be produced at a relative low cost (it starts either from blended elementals or pre-alloyed powders).

MA is the nomenclature for a large number of powder processing methods, operating in solid-state regime, in which, the high-energy ball milling (HEBM) method is the one characterized by severe plastic deformation and ultrafine grinding. In this sense, the HEBM procedure is often used to obtain nanostructured materials [5–8] and\or extended solid solutions [9, 10], consequently can be applied for production of multicomponent materials.

For example, amorphous FeZrB melt-spun ribbons have exhaustively been studied due to their special magnetic properties [5–10]. So, some efforts have also been made to obtain FeZrB amorphous-nanocrystalline alloys, using MA [11, 12]. There also are reports indicating that the addition of Ni in amorphous state of FeZrB materials favors enhancement of their soft magnetic properties when nanostructured materials are obtained [13, 14]. Moreover, from the literature it is well known that nanocrystalline materials (composed of crystalline nanograins dispersed in amorphous matrix) can be produced by following, at least, two different routes (A and B). In Route-A, a melt-spun amorphous ribbon can be subsequently transformed into a NC material (it is called as nanocrystalline) after a controlled thermal treatment [15, 16]. In Route-B, a NC phase can directly be achieved by MA process [17, 18], starting either from pre-alloyed or blended elemental powders. In both routes (A and B), NC materials are assumed to be constituted by ordered phases, with crystalline coherence length in the nanometer-size range due to their grains cores, plus a disordered phase (with a relative large fraction) formed at the grain boundaries [19–21]. The presence of disordered grain boundary phase has been proposed to be responsible for the existence of some interesting properties of these materials [22, 23].

In this work, nanostructured $(Fe_{0.5}Ni_{0.5})_{92}Zr_5B_3$ powder alloy was prepared by high-energy ball mill, using a blend of the pre-alloyed $Fe_{50}Ni_{50}$ precursor (previously prepared) and high purity chemical elemental powders of Zr and B. In a previous work [24], we have reported that the pre-alloyed $Fe_{50}Ni_{50}$ precursor corresponded to a disordered solid solution of fcc γ–$Fe_{45}Ni_{55}$ alloy (91%) and a small fraction of atomically ordered phase of FeNi (9%) having a $L1_0$-like tetragonal structure [24]. These Fe-based phases were identified as taenite (disorder t-FeNi) and tetrataenite (ordered T-FeNi) with grain sizes about 60 nm and 22 nm, respectively. We have been able to demonstrate that the T-FeNi phase, often found in meteorites [phase formed under extreme conditions (temperature and pressure)], can also be prepared by high-energy ball milling. Lee et al. [25], using high-pressure torsion, have also reported the presence of the tetrataenite in the laboratory. In our case, the formation of the T-FeNi phase was attributed to severe plastic deformations that occur during the milling process. Thus, considering that (i) Ni can improve magnetic properties of FeZrB materials and (ii) it has previously been prepared the Fe–Ni NC material [24], in this work, we aimed to prepare nanostructured FeNiZrB alloy using HEBM. Changes on Fe and Ni local environments were systematically studied by extended X-ray absorption fine structure (EXAFS), whereas the ^{57}Fe Mössbauer spectroscopy (MS) was applied to

investigate magnetic ordering and Fe-phases that have occurred in milled samples. Structural information, such as coordination numbers, nearest distance, and mean deviation of distances of Fe and Ni positions (obtained from EXAFS) were used to understand the Fe and Ni arrangements inside the grains of the ordered and disordered phases.

2 Experimental procedure

2.1 Sample preparation

The samples were mechanically synthesized in two steps. $Fe_{50}Ni_{50}$ precursor alloy was firstly obtained after 30 h of milling process, as detailed in Ref. [24]. Then, a mixture of the pre-alloyed $Fe_{50}Ni_{50}$ precursor and high-purity elemental powders of Zr (99.7 + %, below 150 μm) and B (98 + %, below 10 μm) was used to prepare FeNiZrB powder alloys by high-energy ball milling. All milled samples were synthetized in a vibratory ball mill SPEX 8000 unit. Before starting the milling process, the blended powders [precursor (90 *at.* % $Fe_{0.5}Ni_{0.5}$) plus chemical elemental powders (7 *at.* % Zr, 3 *at.* % B)] was sealed in a flat-ending SPEX mill container together with five stainless steel balls (13 mm diameter) under argon atmosphere to reduce severe powder oxidation. The sample manipulation and sealing procedure of the container were also performed inside a steel box under argon gas flow. We have used a ball-to-powder weight ratio of 8:1. The container and the balls are made of the same materials and have the same hardness. The ball-mill unit shakes the grinding container back and forth approximately 1080 cycles per minute. To avoid high temperatures during the ball-milling process, the MA experiment was periodically stopped every 30 min and was restarted after 10 min of pause (when the sample reached room temperature – RT). At pre-defined milling times, small portions of milled samples were collected from the mill container for structural (XRD and EXAFS) and hyperfine (^{57}Fe Mössbauer) analysis.

2.2 X-ray diffraction

Powder X-ray diffraction (XRD) technique, employing a Bruker-D8 Focus diffractometer at 40 kV and 40 mA with Cu-Kα radiation ($\lambda = 1.5406$ Å), was used to studied the effect of MA on bulk structural properties of the milled powders. To determine the percentage of the phases as well as the accurate microstructural parameters (cell parameters, grain size and lattice strain) of the milled crystalline phases, the XRD patterns were analyzed by Rietveld method using Topas software (Bruker AXS) [26].

2.3 X-ray absorption spectroscopy

RT EXAFS measurements were performed at the D04B-XAS beam line of the Brazilian Synchrotron Light Laboratory (LNLS), using Si (111) monochromator. EXAFS spectra were recorded at Fe K-edge (~7112 eV) and at Ni K-edge (~8333 eV). Pure Fe and Ni metals were used as standard samples (energy calibration) for the Fe and Ni K-edge EXAFS spectra, respectively. Data analysis was carried out using IFEFFIT and DEMETER programs [27, 28], following the standard procedures described in Ref. [29]. A standard fitting procedure was computed with FEFF6 program [30, 31]. Information about the local atomic

environments around central absorbing atoms (Fe or Ni), coordination numbers (**N**), the nearest neighbor distances (**R**) and mean deviation of distances (**σ**) of the absorbing atoms were found from the Fourier transform |χ(R)| of the EXAFS oscillation curves. It should be mentioned that the EXAFS method is more sensitive to local structures around absorbing atoms. Thus, it is not appropriated to define long-range order features; because of the mean-free-path of the photoelectrons is typically less than 10 Å [32].

2.4 ^{57}Fe Mössbauer spectroscopy

Fe hyperfine parameters of milled samples were studied by RT transmission ^{57}Fe Mössbauer spectra recorded with a 25 mCi ^{57}Co/Rh radioactive source moving in constant acceleration. In order to obtain the hyperfine parameters [isomer shift (δ), quadrupole shift (2ε), hyperfine magnetic field (B_{hf}), line width (Γ) and relative absorption area (RAA)] of Fe sites, the RT Mössbauer spectra were fitted using NORMOS program with set of sextets (crystalline phases) plus a distribution of magnetic hyperfine fields (B_{hf}). The δ-values of different Fe phases are quoted relatively to RT α-Fe value.

3 Results and discussion

3.1 Rietveld analysis of the XRD pattern of milled $(Fe_{0.5}Ni_{0.5})_{90}Zr_7B_3$ powders

XRD patterns of the pre-alloyed $Fe_{50}Ni_{50}$ powder and the milled $(Fe_{0.5}Ni_{0.5})_{90}Zr_7B_3$ powders milled for 3 (M-3 h), 15 (M-15 h), 21 (M-21 h) and 30 h (M-30 h) are displayed in Fig. 1. The Bragg peaks of the precursor (at the bottom of Fig. 1) due to the disordered fcc γ–(Fe,Ni) and the T-FeNi (small fraction) remain in the XRD patterns of all milled samples, suggesting that the long-range order symmetry did not change with Zr and B additions during the milling process, at least, within our X-ray resolution (no incorporation of these elements in the ordered T-FeNi phase was detected). It is also important to mention that no bcc-like (Fe,Ni) phase has been observed, as suggested by some reported in the literature for different Fe concentration [33]. On the other hand, the Bragg peaks became broader with the increase of milling time and they showed a shifting of about 0.13º to lower angular positions, indicating an increase of the lattice parameter of the disorder t-FeNi phase [fcc γ–(Fe,Ni)]. Thus, it should be attributed to insertion of Zr atoms (large atomic radius) in the disorder t-FeNi. However, considering that the Zr-oxide phase was observed after 15 h of milling, only part of the nominal Zr concentration (~5%) was incorporated in the disorder t-FeNi matrix. The weight percentages of Zr-oxide (ZrO_2) and Zr in the M-30 h sample and in the blended (M-0 h) sample, theoretically calculated from Rietveld refinement, were respectively 5 and 11%. From this analysis, it was estimated that 63(1) weight percentage of Zr (not oxidized) were incorporated in the disorder t-FeNi phase.

Thus, based on previous results of the pre-alloyed $Fe_{50}Ni_{50}$ precursor, the XRD patterns of the M-3 h, M-15 h, M-21 h and M-30 h samples were analyzed considering the two crystalline Fe–Ni phases previously discussed [24], but now with Zr and B atoms incorporating in the disorder t-FeNi matrix. Figure 2(a) and (b) displays, for example, the measured and calculated XRD patterns of the pre-alloyed $Fe_{50}Ni_{50}$ precursor and the M-30 h sample, respectively. Table 1 presents the Rietveld refinement results, where structural parameters [cell parameters, grain size $<D>$, mean microstrain ($<\varepsilon^2>^{1/2}$), atomic occupancy (Ocp) and phase percentage (x_{ph})] are shown for

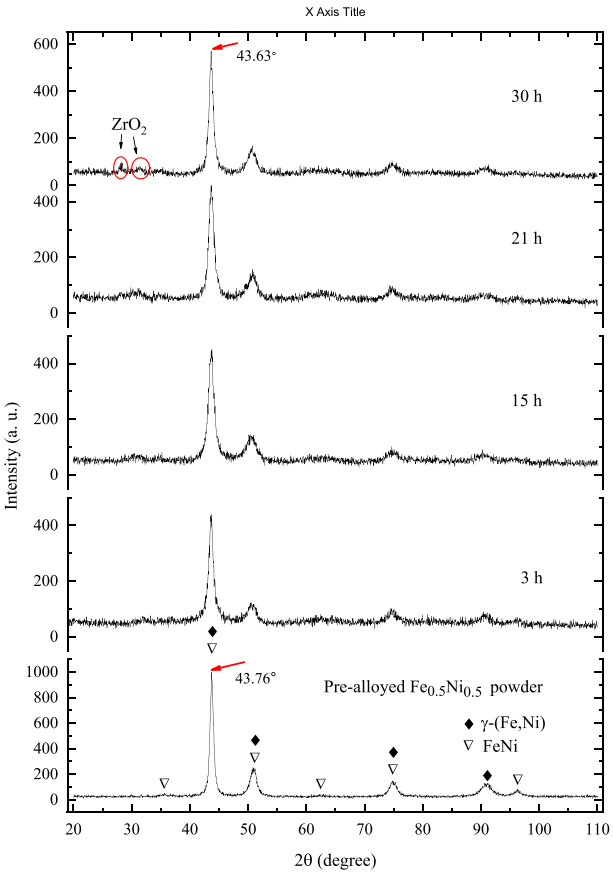

Fig. 1 X-ray diffraction (XRD) patterns of the $(Fe_{0.5}Ni_{0.5})_{90}Zr_7B_3$ milled powders for the indicated milling times. XRD pattern of the precursor $Fe_{0.5}Ni_{0.5}$ alloy is also shown for comparison

the milled samples and pre-alloyed precursor. In a first approximation, the fit results suggested that Fe and Ni atoms share 4*a* Wyckoff site in the fcc phase, confirming the chemical disorder character of the γ–(Fe,Ni) phase ($Ocp^{Fe} \approx 0.48$, $Ocp^{Ni} \approx 0.52$), i.e., the γ–$Fe_{48}Ni_{52}$ should be associated with the chemically disordered t-FeNi alloy. The microstrains at the interval between 0.25 to 0.40% (calculated for this disordered fcc phase in all samples) are in agreement with typical values for distorted fcc-type lattices [14]. The presence of atoms of different sizes induces internal strain into the lattice [34]. The T-FeNi phase, with 6% of the total area of the XRD pattern, indicated a reduction of 33% of this phase as compared with the pre-alloyed precursor sample [24]. No significant change of average grain sizes (<D>) of these FeNi phases was observed up to 30 h of milling time.

From the XRD analysis, it can be partially inferred that the M-30 h sample corresponds to a nanostructured $(Fe_{0.5}Ni_{0.5})_{92}Zr_5B_3$ powder alloy, i.e., a material composed of a dominant contribution of disordered solid solution of fcc γ–FeNiZrB alloy (89%), small fraction of atomically ordered phase of FeNi (6%) plus ZrO_2 (5%), all with grain sizes in nanometer regime.

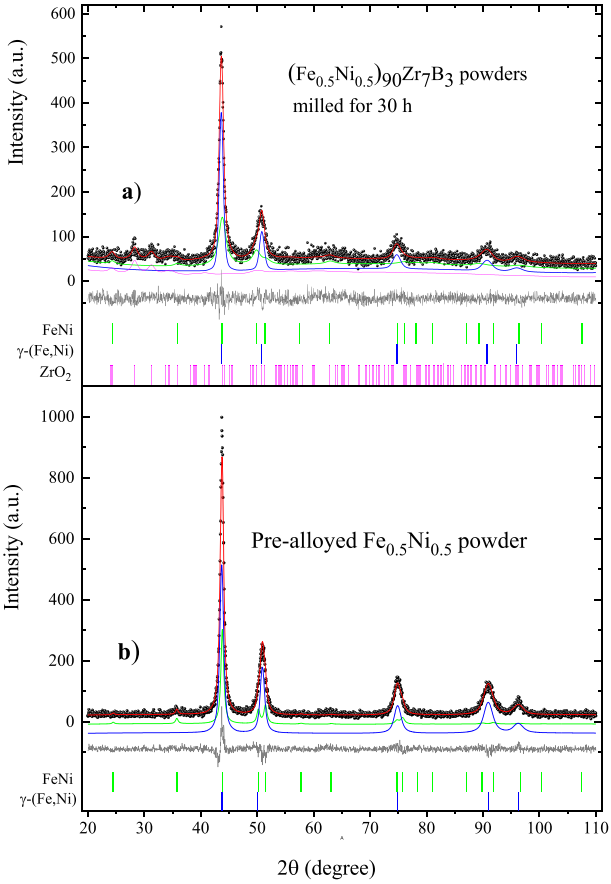

Fig. 2 Rietveld refinement of the X-ray diffraction patterns of the: (**a**) pre-alloyed $Fe_{0.5}Ni_{0.5}$ and (**b**) $(Fe_{0.5}Ni_{0.5})_{90}Zr_7B_3$ sample milled for 30 h. The difference between observed and calculated patterns, and the calculated reflection positions (bottom trace) are also displayed

3.2 Structural properties analyzed by EXAFS measurements

The EXAFS oscillation curves for the M-30 h sample and the corresponding Fourier transform $|\chi(R)|$ of the Fe and Ni K-edges are respectively plotted in Figs. 3(a) and (b). The Fe and Ni Fourier transforms $|\chi(R)|$ of the EXAFS oscillations curves (inset figures) have broad and asymmetric main peaks at about 2.2 Å and 2.5 Å, respectively. They are associated with the first coordination shells around each absorbing atoms (Fe or Ni). To determine the structural parameters ($\mathbf{N}_j$, $\mathbf{R}_j$ and $\boldsymbol{\sigma}_j$) of the M-30 h sample, the main peak of the Fourier transform $|\chi(R)|$ curve was fitted in the Hanning window, as indicated in Figs. 4(a) and (b). Outside the Hanning window, no medium-range order (around Fe and Ni sites) was seen; an observation that is also reflecting the nanocomposite character of the M-30 h sample. The peaks below 1.5 Å [red arrows in Figs. 4(a) and (b)] are related to a low-frequency problem of the background (it has no physical meaning).

In order to prepare an initial model for the fits of the EXAFS spectra, the previous XRD results were used, i.e., the presence of disordered fcc taenite (t-FeNi) and chemically ordered tetrataenite (T-FeNi) phases. In addition, considering that Fe and Ni atoms share the same atomic site for the t-FeNi contribution, a model with one shell was applied. Otherwise, for the T-FeNi contribution, a model assuming two shells was used due to the

Table 1 Structural parameters obtained from Rietveld refinement of XRD patterns of the pre-alloyed $Fe_{0.5}Ni_{0.5}$ powder and the milled $(Fe_{0.5}Ni_{0.5})_{90}Zr_7B_3$ samples (cell parameters, grain size $<D>$, mean microstrain ($<\varepsilon^2>^{1/2}$), atomic occupancy (Ocp), and phase percentage (X_{ph}))

Sample	Phase	Space group	Atom	Wyckoff site	Ocp	Cell parameters			$<D>$ (nm)	$<\varepsilon^2>^{1/2}$ (%)	X_{ph} (%)
						a (Å)	b (Å)	c (Å)			
Pre-alloy $Fe_{0.5}Ni_{0.50}$	FeNi	P4/mmm	Fe	1*a*	1.00	2.50(1)	2.50(1)	3.63(1)	22(3)	0.15(3)	9(2)
			Ni	1*d*	1.00						
	γ-(Fe,Ni)	Fm $\bar{3}$ m	Fe	4*a*	0.45	3.58(2)	3.58(2)	3.58(2)	60(3)	0.25(3)	91(2)
			Ni	4*a*	0.55						
$(Fe_{0.5}Ni_{0.5})_{90}Zr_7B_3$ 3 h	FeNi	P4/mmm	Fe	1*a*	1.00	2.50(2)	2.50(2)	3.62(2)	20(4)	0.18(3)	8(2)
			Ni	1*d*	1.00						
	γ-(Fe,Ni)	Fm $\bar{3}$ m	Fe	4*a*	0.45	3.59(4)	3.59(4)	3.59(4)	60(4)	0.40(4)	92(2)
			Ni	4*a*	0.55						
$(Fe_{0.5}Ni_{0.5})_{90}Zr_7B_3$ 15 h	FeNi	P4/mmm	Fe	1*a*	1.00	2.50(3)	2.50(3)	3.65(1)	20(4)	0.47(5)	7(2)
			Ni	1*d*	1.00						
	γ-(Fe,Ni)	Fm $\bar{3}$ m	Fe	4*a*	0.46	3.59(4)	3.59(4)	3.59(4)	60(5)	0.34(4)	93(2)
			Ni	4*a*	0.54						
$(Fe_{0.5}Ni_{0.5})_{90}Zr_7B_3$ 21 h	FeNi	P4/mmm	Fe	1*a*	1.00	2.50(2)	2.50(2)	3.65(4)	20(3)	0.45(8)	6(2)
			Ni	1*d*	1.00						
	γ-(Fe,Ni)	Fm $\bar{3}$ m	Fe	4*a*	0.46	3.58(3)	3.58(3)	3.58(3)	60(4)	0.32(5)	91(2)
			Ni	4*a*	0.54						
	ZrO_2	P21/c	Zr	4*e*	1.00	5.18(3)	4.9(8)	5.18(7)	92(8)	0.86(5)	3(2)
			O	4*e*	1.00						
			O	4*e*	1.00						
$(Fe_{0.5}Ni_{0.5})_{90}Zr_7B_3$ 30 h	FeNi	P4/mmm	Fe	1*a*	1.00	2.50(2)	2.50(2)	3.65(5)	20(5)	0.42(6)	6(2)
			Ni	1*d*	1.00						
	γ-(Fe,Ni)	Fm $\bar{3}$ m	Fe	4*a*	0.48	3.59(4)	3.59(4)	3.59(4)	60(8)	0.30(5)	89(2)
			Ni	4*a*	0.52						
	ZrO_2	P21/c	Zr	4*e*	1.00	5.18(4)	5.10(4)	5.22(4)	86(8)	0.82(6)	5(2)
			O	4*e*	1.00						
			O	4*e*	1.00						

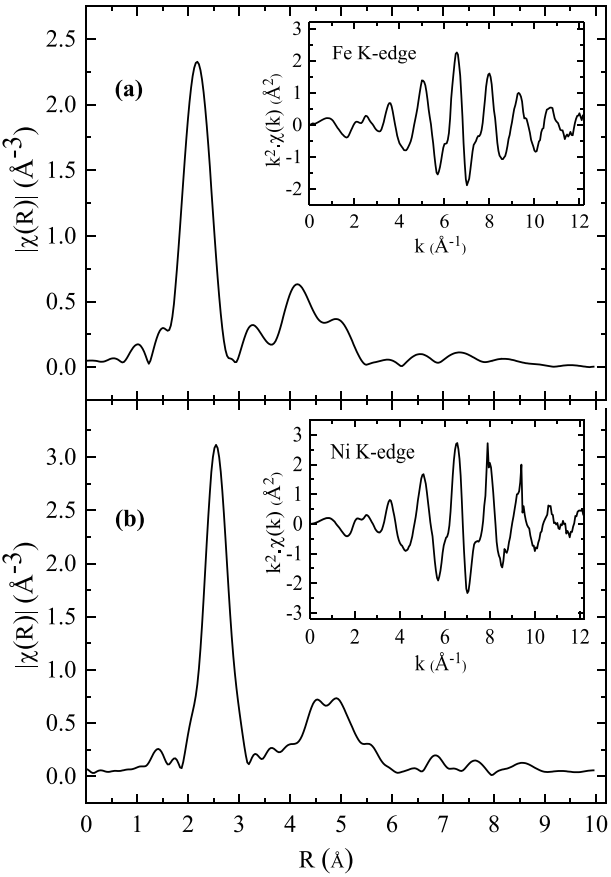

Fig. 3 Fourier transforms of the Fe K-edge EXAFS (**a**) and Ni K-edge EXAFS (**b**) spectra obtained for the $(Fe_{0.5}Ni_{0.5})_{90}Zr_7B_3$ sample milled for 30 h, as indicated. Inset figures show the corresponding EXAFS oscillations curves

tetragonal configuration of this phase. Figure 5(a) and (b) presents a schematic representation of the first shells of coordination around absorbing atoms (Fe or Ni) for the unit cells of the t-FeNi and T-FeNi, respectively.

An EXAFS analysis of multicomponent samples is a hard task due to strong correlation among the local structural parameters. In the fitting model, Fe, Ni and Zr atoms are considered distinguishable backscatters, whereas B atoms were assumed to have low contribution, i.e., it has small backscattering amplitude relatively to Fe and Ni scattering factors. Additionally, considering the chemical disorder character of the fcc γ–FeNiZrB alloy, we assumed in the fitting model a low contribution from Zr incorporations into the first coordination of Fe and Ni absorbing atoms. Thus, the individual contributions (within the first shells) of Fe–Fe and Fe–Ni pairs and Ni–Fe and Ni–Ni pairs to the Fourier transform of the Fe and Ni K-edge EXAFS spectra of the M-30 h sample are respectively shown in Figs. 4(a) and (b). Moreover, for the fit of the EXAFS spectra, the Fe-B and Ni–B pair contributions were assumed indistinguishable in the shell; an assumption supported by the low B concentration in the M-30 h sample. Table 2 displays the structural parameter values ($\mathbf{N}_j$, $\mathbf{R}_j$ and $\boldsymbol{\sigma}_j$), including the phase percentages (X_{pha}) obtained from the EXAFS data analysis of the M-30 h sample. These values correspond to average values over different sites of absorbing atoms (Fe or Ni).

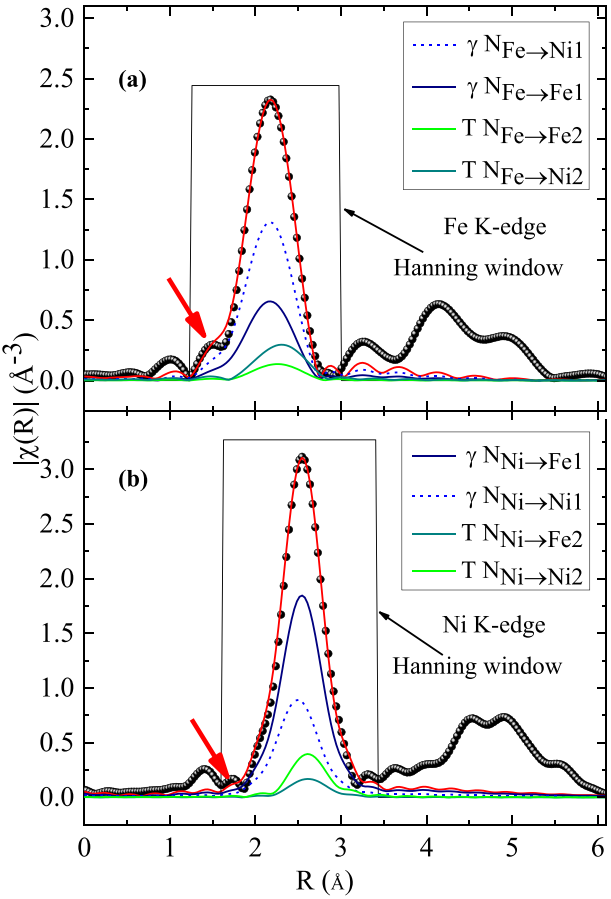

Fig. 4 First (1st) shell analyses: individual contributions of (**a**) Fe–Fe and Fe–Ni pairs from the Fourier transform of the Fe K-edge EXAFS spectra and (**b**) Ni–Fe and Ni–Ni pairs from Fourier transform of the Ni K-edge EXAFS spectra for the $(Fe_{0.5}Ni_{0.5})_{90}Zr_7B_3$ powder milled for 30 h (30 h sample)

From the Fe K-edge EXAFS spectrum of the M-30 h sample, an average **N**-value of 11.1 atoms ($\mathbf{N}_{Fe-Fe_1} + \mathbf{N}_{Fe-Ni_1} = 3.7$ Fe atoms + 7.4 Ni atoms = 11.1 atoms) was found for the first shell, while a N-value of 10.8 atoms ($\mathbf{N}_{Ni-Ni_1} + \mathbf{N}_{Ni-Fe_1} = 7.4$ Ni atoms + 3.4 Fe atoms = 10.8 atoms) was calculated for the Ni K-edge EXAFS spectrum in the disordered γ–(Fe,Ni) phase. Both N-values are below 12, which is the expected **N**-value for the Fe and Ni in fcc ordered phases. This result suggests that the difference in N-values, in principle, can be attributed to the chemical disorder around Fe and Ni absorbing atoms and\or due to the Zr and B incorporations. The atomic percentage of the Fe and Ni atoms in the γ–(Fe,Ni) phase are 39% and 61%, respectively. This composition agrees with the composition range found in the literature [35, 36]. In addition, the $\boldsymbol{\sigma}_{Fe\text{-}Fe}$ and $\boldsymbol{\sigma}_{Fe\text{-}Ni}$ values are also found in disordered alloys [37]. Therefore, the results here presented are in good agreement with existence of a disordered fcc solid solution model for the γ–(Fe,Ni) phase in the M-30 h sample (the main contribution for the EXAFS spectra).

For the T-FeNi phase, two shells for the main peak of the Fourier transform |χ(R)| curve were considered. **N**-values equal to 3.6 and 7.8 were respectively obtained for the 1st ($\mathbf{N}_{Fe\text{-}Fe2}$) and 2nd-shell ($\mathbf{N}_{Fe\text{-}Ni2}$) of the Fe absorber in the M-30 h sample. For the Ni absorber, the **N**-value is 3.5 for the 1st-shell ($\mathbf{N}_{Ni\text{-}Ni2}$) and 7.5 for the Ni 2nd-shell ($\mathbf{N}_{Ni\text{-}Fe2}$).

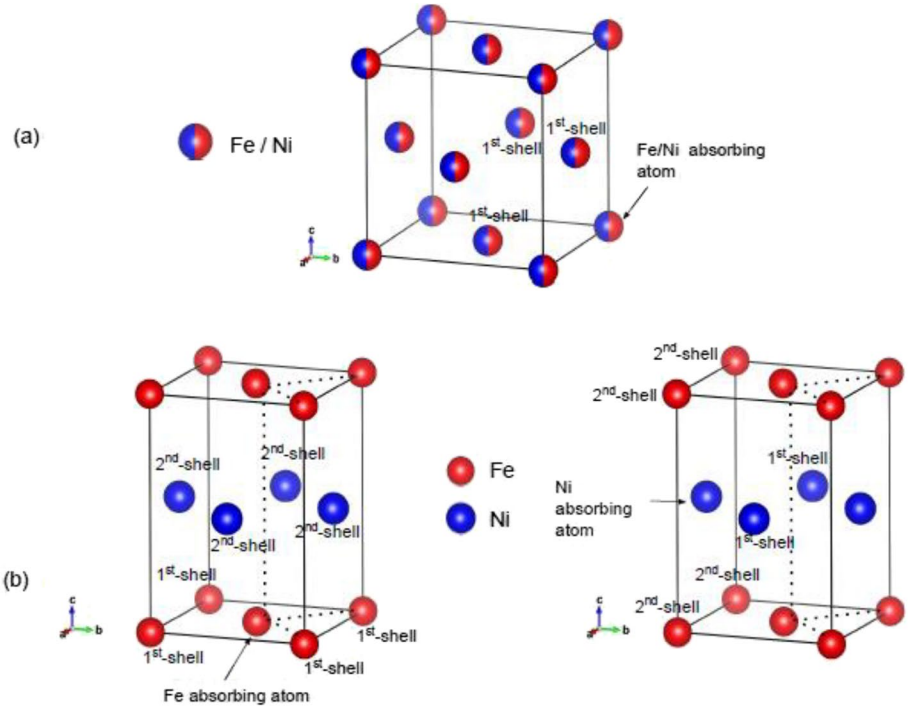

Fig. 5 Unit cells of the taenite: t-FeNi (**a**) and tetrataenite: T-FeNi (**b**) phases. Taenite has the fcc structure ($Fm\,\overline{3}\,m$, where Fe and Ni atoms share 4*a* Wyckoff site), whereas the tetrataenite has the $L1_0$ tetragonal structure ($P4/mmm$, where Fe and Ni atoms are both on 1*a* and 1*d* Wyckoff sites)

These **N**-values (first and second shells) are close to those ones (4 and 8) found for the tetragonal ordered equiatomic FeNi phase [38]; results that suggest no Zr and B substitutions in the thermodynamically stable T-FeNi phase. They also give evidences about small changes in the chemical short-range order around Fe and Ni atoms that occurred in the M-30 h sample. In contrast, the low fluctuation of the interatomic distances ($\boldsymbol{\sigma}_{\text{Fe-Fe}}$, $\boldsymbol{\sigma}_{\text{Fe-Ni}}$, $\boldsymbol{\sigma}_{\text{Ni-Ni}}$ and $\boldsymbol{\sigma}_{\text{Ni-Fe}}$) in the 1st-coordination (around Fe and Ni absorbing atoms) reflects no changes on the topological short-range order. The nearest distances (Table 2) between Fe and Ni atoms ($\mathbf{R}_{\text{Fe-Fe}}$, $\mathbf{R}_{\text{Fe-Ni}}$, $\mathbf{R}_{\text{Ni-Ni}}$ and $\mathbf{R}_{\text{Ni-Fe}}$) in the M-30 h sample are also in good agreement with the cell parameter values obtained from the XRD data. Thus, it was demonstrated (from the XRD and EXAFS results) a structural stability for the milled material. In addition, milled powders have kept the nanocomposite character of the precursor, where the ordered FeNi phase is dispersed, in principle, at the grain boundaries of the disordered FeNi phase now with B and Zr substitutions (37 weight percentage of Zr was converted in the ZrO_2 phase).

3.3 Hyperfine magnetic properties studied by Mössbauer spectroscopy

Considering that (i) the milled $(Fe_{0.5}Ni_{0.5})_{92}Zr_5B_3$ alloy has Fe-rich phases and (ii) Mössbauer spectroscopy can be very sensitive to changes on Fe environments by measuring their hyperfine interactions, so local Fe environment changes were systematically studied by

Table 2 Structural parameters obtained from EXAFS analysis of the milled 30 h-$(Fe_{0.5}Ni_{0.5})_{90}Zr_7B_3$ sample (coordination numbers ($\mathbf{N}_j$), nearest distance ($\mathbf{R}_j$), mean deviation ($\boldsymbol{\sigma}_j$) of distances of the absorbing atoms for each shell j and phase percentage (X_{pha}))

Sample	Edge	Phase	Shell	Absorbing atom-Scattering atom	**R** (Å)	**N**	$\boldsymbol{\sigma}^2$ (Å^2)	X_{pha} (%)
$Fe_{0.5}Ni0_{.5}$	Fe K_α	γ-(Fe,Ni)	1	Fe → Fe1	2.53(1)	3.8(2)	0.008(2)	91(2)
				Fe → Ni1	2.53(1)	7.3(2)	0.006(2)	
		FeNi	1	Fe → Fe2	2.53(1)	3.4(2)	0.003(2)	9(2)
			2	Fe → Ni2	2.56(1)	7.9(2)	0.007(2)	
	Ni K_α	γ-(Fe,Ni)	1	Ni → Ni1	2.53(1)	7.5(2)	0.010(2)	92(2)
				Ni → Fe1	2.48(1)	3.2(2)	0.004(2)	
		FeNi	1	Ni → Ni2	2.53(1)	3.6(2)	0.005(2)	8(2)
			2	Ni → Fe2	2.55(1)	7.6(2)	0.005(2)	
$(Fe_{0.5}Ni0_{.5})_{90}Zr_7B_3$	Fe K_α	γ-(Fe,Ni)	1	Fe → Fe1	2.55(1)	3.7(2)	0.014(3)	92(2)
			1	Fe → Ni1	2.54(1)	7.4(2)	0.014(3)	
		FeNi	1	Fe → Fe2	2.54(1)	3.6(2)	0.006(3)	8(2)
			2	Fe → Ni2	2.55(1)	7.8(2)	0.005(3)	
	Ni K_α	γ-(Fe,Ni)	1	Ni → Ni1	2.54(1)	7.4(2)	0.011(3)	92(2)
			1	Ni → Fe1	2.52(1)	3.4(2)	0.011(3)	
		FeNi	1	Ni → Ni2	2.53(1)	3.7(2)	0.005(3)	8(2)
			2	Ni → Fe2	2.55(1)	7.5(2)	0.004(3)	

taking RT transmission ^{57}Fe Mössbauer spectra at different milling times (M-0 h, M-3 h, M-15 h M-21 h and M-30 h). The RT Mössbauer spectra (Fig. 6) display broad six-line patterns due to nuclear Zeeman interaction [magnetic hyperfine field (B_{hf}) at Fe nucleus]. It indicates that Fe atoms are placed in non-equivalent magnetic sites. To fit these spectra the following conditions were assumed: (i) two magnetic components; the disordered fcc FeNiZrB phase [a magnetic hyperfine field distribution block P(B_{hf})] and the ordered FeNi phase (sextet); the latter one found in XRD and EXAFS data, (ii) a linear correlation between B_{hf} and δ of 40 magnetic sub-spectra to account for small asymmetries of the spectra and (iii) a new sextet associated with the formation of Fe-B alloy (these elements have great chemical affinity).

The magnetic hyperfine field distribution P(B_{hf}) curves are plotted at the right-hand side of the Fig. 6. The obtained hyperfine parameter values [δ, quadrupole shifting (2ε), hyperfine magnetic field (B_{hf}), linewidth (Γ) and relative absorption area (RAA)] are listed in Table 3.

From the fitting, it is observed that:

a) The P(B_{hf}) distribution component dominates over the crystalline sextets for all milled samples. Hyperfine parameters of the distribution component still keep values close to those reported in the literature for the taenite phase (t-FeNi) [39, 40], but some small changes have occurred during milling process (e.g., the average B_{hf} value shifts from 29.9 T to lower field range around 29.1 T) due to Zr and B inclusions. Moreover, the near zero δ-values (relative to α-Fe) and the simetric absorption peaks of the magnetic distribution reflect that Fe atoms are in Fe-rich phase with cubic-like symmetry (vanished quadrupole splitting). Thus, this component can be attributed to iron sites in chemically disordered phase of fcc γ–(Fe,Ni) or simply taenite (t-FeNi) where the Zr and B atoms

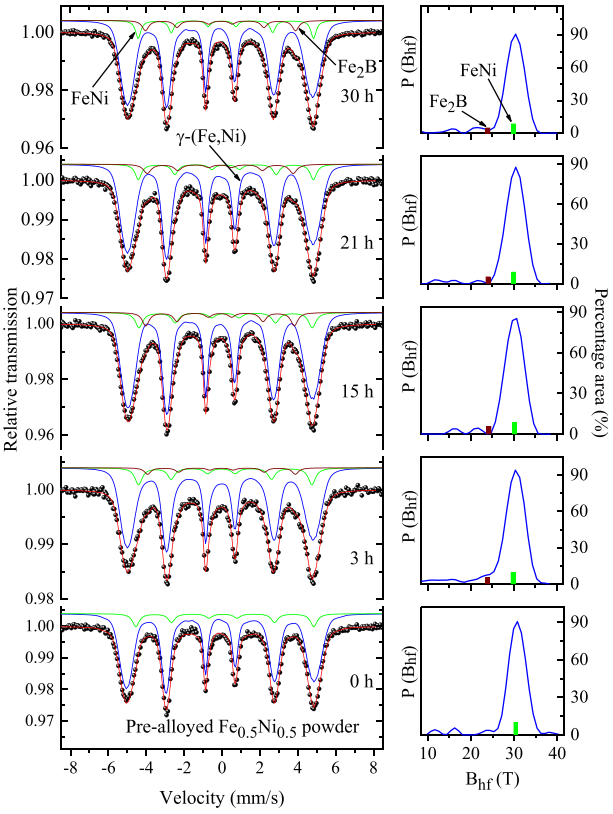

Fig. 6 RT Mössbauer spectra for the $(Fe_{0.5}Ni_{0.5})_{90}Zr_9B_3$ powders recorded at different milling times (MT), as indicated. Magnetic hyperfine field distribution $P(B_{hf})$ curves, obtained from the fits of the corresponding Mössbauer spectra, are plotted on the right-hand side of this figure. The bars inside the $P(B_{hf})$ correspond to the relative intensity (%) of Fe_2B and T-FeNi phase

are entering in lattice defects of grain boundaries and form a soft magnetic matrix, as expected for the disordered fcc FeNiZrB phase [14];

b) The sextet can be attributed (green absorption six lines) to the T-FeNi, since its hyperfine parameter values (Table 3) match with values reported for the ordered FeNi phase [40–42]. No change of the T-FeNi hyperfine parameters was observed during milling process; an effect that confirms the fact that the T-FeNi is a thermodynamically stable phase (its relative fraction has reduced with the increase of milling time);

c) For milling time larger and equal than 3 h, the Mössbauer spectra have their shapes slightly modified due to the formation of Fe_2B phase [43]; assumed to be stabilized by boron inclusion at defects of the Fe–Ni grain boundaries (the boron insertion process favors segregation of a more stable phase, i.e., the Fe_2B phase). The apparent absence of the Fe_2B phase in the XRD pattern can be attributed to nanometric order size of the grains and its low fraction (it may be dispersed at the XRD pattern background).

From the results here discussed, it can be inferred that the $(Fe_{0.5}Ni_{0.5})_{92}Zr_5B_3$ nanocomposite alloy (M-30 sample) is basically formed by magnetic Fe–Ni rich phases: the ordered FeNi (8%) and Fe_2B (6%) nanocrystals immersed in disordered fcc solid solution of FeNiZrB matrix (86%) rich in nickel. The presence of magnetically ordered phases (T-FeNi and Fe_2B) could be important for further studies, for example, where

Table 3 Hyperfine parameters values of the milled $(Fe_{0.5}Ni_{0.5})_{90}Zr_7B_3$ samples obtained from Mössbauer spectra fitting (isomer shift (δ), quadrupole shift (2ε), hyperfine magnetic field (B_{hf}), line width (Γ) and relative absorption area (RAA)). The δ values are given relative to α-Fe obtained at room temperature

MT (h)	Phase	Crystalline sites			Γ (mm/s)	Magnetic distribution		(RAA) (%)
		δ (mm/s)	B_{hf} (T)	2ε (mm/s)		$<\delta>$ (mm/s)	$<B_{hf}>$ (T)	
0	FeNi	0.143(5)	28.9(3)	0.09(2)	0.37(2)	—	—	10(2)
	γ-(Fe,Ni)	—	—	—	—	0.017(8)	29.9(2)	90(2)
1	FeNi	0.146(5)	29.5(5)	0.10(5)	0.37(2)	—	—	10(2)
	γ-(Fe,Ni)	—	—	—	—	0.017(8)	29.8(2)	90(2)
3	FeNi	0.145(5)	28.4(3)	0.10(5)	0.38(2)	—	—	10(2)
	Fe_2B	0.048(8)	24.3(4)	—	0.40(2)	—	—	3(3)
	γ-(Fe,Ni)	—	—	—	—	0.004(7)	28.7(3)	87(2)
9	FeNi	0.148(5)	28.3(2)	0.10(5)	0.37(2)	—	—	9(2)
	Fe_2B	0.058(5)	24.3(2)	—	0.40(2)	—	—	4(2)
	γ-(Fe,Ni)	—	—	—	—	0.006(8)	29.8(2)	87(2)
15	FeNi	0.147(5)	28.3(2)	0.010(5)	0.37(2)	—	—	8(2)
	Fe_2B	0.054(5)	24.3(2)	—	0.40(2)	—	—	6(2)
	γ-(Fe,Ni)	—	—	—	—	0.008(8)	29.0(2)	86(2)
21	FeNi	0.146(5)	28.6(2)	0.010(5)	0.37(2)	—	—	8(2)
	Fe_2B	0.054(5)	24.3(2)	—	0.40(2)	—	—	6(2)
	γ-(Fe,Ni)	—	—	—	—	0.006(8)	29.0(2)	86(2)
30	FeNi	0.146(5)	28.7(1)	0.010(5)	0.37(2)	—	—	8(2)
	Fe_2B	0.058(5)	24.3(2)	—	0.40(2)	—	—	6(2)
	γ-(Fe,Ni)	—	—	—	—	0.009(8)	29.1(2)	86(2)

magnetic interactions among these magnetic crystals, intermediated by the magnetic FeNiZrB matrix, could be performed.

4 Conclusions

In this work, we have prepared and characterized nanostructured $(Fe_{0.5}Ni_{0.5})_{90}Zr_7B_3$ alloy obtained by milling a blending of pre-alloyed $Fe_{50}Ni_{50}$ precursor and Zr and B elemental powders up to 30 h. From bulk and local structural studies as well as hyperfine investigations, it was demonstrated a structural stability of milled material during the mechanical alloying process. The average grain-size of the samples is practically milling time independent (they are in nanometer regime). EXAFS results have shown small changes of the chemical short range order in disordered fcc γ–(Fe,Ni) phase due to Zr and B inclusions and no changes in structural properties of the ordered equiatomically FeNi phase. Mössbauer data have also suggested (besides the Fe–Ni rich phases in chemically disordered phase) the formation of Fe_2B nanograins; a phase that was stabilized at the Fe–Ni grain boundaries during the milling process due to high chemical affinity of Fe-B when compared with the Fe–Ni. The 30 h milled powdered material has a nanocomposite character, which is composed by two magnetically and atomically ordered phases (T-FeNi and Fe_2B) dispersed at grain boundaries of the chemically disordered fcc FeNiZrB (86% of total area

as shown in Table 1). This nanocomposite material is a good candidate to study magnetic interactions between atomically ordered phases (T-FeNi and Fe_2B) through a soft magnetically disordered phase.

Acknowledgements This work was supported by the Brazilian Synchrotron Light Laboratory (LNLS) under proposal XAFS1 – 1304. The authors would like to acknowledge the financial support provided by the National Fund for Scientific and Technological Development, F*ONDECYT* [contract 011-2014-FONDECYT], FAPERJ-Brazil (Emeritus fellowship, EBS, E26/210.715/2014, E-26/010.002990/2014 grants), FINEP, FAPES, CNPq, and Latin American Center of Physics. The authors would also like to acknowledge the San Marcos National University for providing research facilities and financial support [CSI-projects: 061301011-0801301011-091301031].

CRediT authorship contribution statement V.A. Peña Rodríguez: Conceptualization, Formal analysis, Writing-Original draft preparation, Project administration, Funding acquisition. **J. Medina Medina:** Investigation, Validation, Data curation, Software, Resources. **C. Rojas-Ayala:** Software, Formal analysis, Investigation. **P. Paucar Cabrera:** Investigation. **C.V. Landauro:** Writing, reviewing and editing, Funding acquisition, Visualization. **J. Quispe-Marcatoma:** Investigation, Formal analysis, Resources. **J. Rojas Tapia:** Software, Visualization. **E.M. Baggio-Saitovitch:** Writing, reviewing and editing, Formal analysis, Conceptualization. **E.C. Passamani:** Writing, reviewing and editing, Formal analysis, Visualization.

Data availability Data will be made available from the authors on request.

Declarations

Declaration of competing interest The authors declare that they have no significant competing financial, professional, or personal interests in this manuscript submission.

Author agreement The authors declare that this manuscript contains original scientific work and has not been published before elsewhere. All the authors listed have approved the final draft of the manuscript.

References

1. Benjamin, J.S.: Dispersion strengthened super-alloys by mechanical alloying. Metall. Trans. **1**, 2943–2951 (1970). https://doi.org/10.1007/BF03037835
2. Koch, C.C.: Materials Synthesis by Mechanical Alloying. Ann. Rev. Mater. Sci. **19**, 121–143 (1989). https://doi.org/10.1146/annurev.ms.19.080189.001005
3. Zoz, H.: Attritor Technology-Latest Developments. Mater. Sci. Forum **179–181**, 419–424 (1995). https://doi.org/10.4028/www.scientific.net/MSF.179-181.419
4. Basset, D., Matteazzi, P., Mani, F.: Designing a high energy ball-mill for synthesis of nanophase materials in large quantities. Mater. Sci. Eng. A **168**, 149–152 (1993). https://doi.org/10.1016/0921-5093(93)90718-T
5. Miglierini, M., Lančok, A., Kohout, J.: Hyperfine fields in nanocrystalline Fe–Zr–B probed by ^{57}Fe nuclear magnetic resonance spectroscopy. Appl. Phys. Lett. **96**, 211902 (2010). https://doi.org/10.1063/1.3431612
6. Stankov, S., Sepiol, B., Kaňuch, T., Scherjau, D., Würschum, R., Miglierini, M.: High temperature Mössbauer effect study of $Fe_{90}Zr_7B_3$ nanocrystalline alloy. J. Phys. Condens. Matter **17**, 3183–3196 (2005). https://doi.org/10.1088/0953-8984/17/21/013
7. Suzuki, K., Makino, A., Inoue, A., Masumoto, T.: Soft magnetic properties of nanocrystalline bcc Fe-Zr-B and Fe-M-B-Cu (M=transition metal) alloys with high saturation magnetization (invited). J. Appl. Phys. **70**, 6232–6237 (1991). https://doi.org/10.1063/1.350006
8. Świerczek, J.: Medium range ordering and some magnetic properties of amorphous $Fe_{90}Zr_7B_3$ alloy. J. Magn. Magn. Mater. **322**, 2696–2702 (2010). https://doi.org/10.1016/j.jmmm.2010.04.010
9. Świerczek, J., Mydlarz, T.: Magnetic entropy changes at early stages of nanocrystallization in amorphous $Fe_{90}Zr_7B_3$ ribbons. J. Alloy. Compd. **509**, 9340–9345 (2011). https://doi.org/10.1016/j.jallcom.2011.07.033

10. Gao, Y., Shindo, D., Bitoh, T., Makino, A.: Domain structures of nanocrystalline $Fe_{90}Zr_7B_3$ alloy studied by Lorentz microscopy. Sci. Tech. Adv. Mater. **4**, 353–359 (2003). https://doi.org/10.1016/j.stam.2003.09.001
11 Hua, Z., Sun, Y.M., Yu, W.Q., Wei, M.B., Liu, L.H.: Preparation and properties of FeZrB amorphous-nanocrystalline soft magnetic alloy. J. Wuhan Univ. Technol. Mat. Sci. Edit. **24**, 747–749 (2009). https://doi.org/10.1007/s11595-009-5747-4
12. Hua, Z., Sun, Y.M., Yu, W.Q., Wei, M.B., Liu, L.H.: Structure and magnetic properties of $Fe_{88-x}Zr_xB_{12}$ (x = 5, 10, 20) alloys prepared by mechanical alloying. J. Alloy. Compd. **477**, 529–531 (2009). https://doi.org/10.1016/j.jallcom.2008.10.075
13 Saravanan, T.T., Kumaran, S., Srinivasa Rao, T.: Structural evolution and magnetic properties of mechanically alloyed metastable Fe–Ni–Zr–B system. Mater. Lett. **63**, 780–782 (2009). https://doi.org/10.1016/j.matlet.2009.01.003
14. Suñol, J.J., González, A., Bonastre, J., Clavaguera-Mora, M.T., Arcondo, B.: Synthesis and characterization of nanocrystalline FeNiZrB developed by mechanical alloying. J. Alloy. Compd. **434–435**, 415–419 (2007). https://doi.org/10.1016/j.jallcom.2006.08.319
15. Suzuki, K., Kataoka, N., Inoue, A., Makino, A., Masumoto, T.: High Saturation Magnetization and Soft Magnetic Properties of bcc Fe–Zr–B Alloys with Ultrafine Grain Structure. Mater. Trans. JIM **31**(8), 743–746 (1990). https://doi.org/10.2320/matertrans1989.31.743
16. Yoshizawa, Y., Oguma, S., Yamauchi, K.: New Fe-based soft magnetic alloys composed of ultrafine grain structure. J. Appl. Phys. **64**, 6044–6046 (1988). https://doi.org/10.1063/1.342149
17. Pereira, R.D., Passamani, E.C., Larica, C., Freitas, J.C.C., Takeuchi, A.Y.: Nanostructured FeZrCuB alloys prepared by mechanosynthesis. J. Appl. Phys. **102**, 033515 (2007). https://doi.org/10.1063/1.2768009
18. Peña Rodríguez, V.A., Quispe Marcatoma, J., Rojas Ayala, Ch., Baggio-Saitovitch, E.M., Passamani, E.C.: Local environments of Fe and Co in $(Fe_{0.5}Co_{0.5})_{75}Si_{15}B_{10}$ mechanically alloyed. J. Alloy. Compd. **475**, 29–34 (2009). https://doi.org/10.1016/j.jallcom.2008.07.104
19. Guérault, H., Bureau, B., Silly, G., Buzaré, J.Y., Grenèche, J.M.: Local structural orders in nanostructured fluoride powders. J. Non Cryst. Solids **287**(1–3), 65–69 (2001). https://doi.org/10.1016/S0022-3093(01)00541-5
20. Herr, U., Jing, J., Birringer, R., Gonser, U., Gleiter, H.: Investigation of nanocrystalline iron materials by Mössbauer spectroscopy. Appl. Phys. Lett. **50**, 472–474 (1987). https://doi.org/10.1063/1.98177
21. Grafouté, M., Labaye, Y., Calvayrac, F., Grenèche, J.M.: Structure of grain boundaries in nanostructured powders: a Monte-Carlo/EAM numerical investigation. Eur. Phys. J. B **45**, 419–424 (2005). https://doi.org/10.1140/epjb/e2005-00199-x
22. Herzer, G.: Nanocrystalline soft magnetic alloys. In: Handbook of Magnetic Materials, Vol. 10, Chapter 3, 415–462. Elsevier Science, Amsterdam (1997)
23. Pillaca Quispe, M., Landauro, C.V., Pinto Vergara, M.Z., Quispe-Marcatoma, J., Rojas-Ayala, C., Peña-Rodríguez, V.A., Baggio-Saitovitch, E.M.: Influence of high energy milling on the microstructure and magnetic properties of the Al–Cu–Fe phases: the case of the i-$Al_{64}Cu_{23}Fe_{13}$quasicrystalline and the ω-$Al_{70}Cu_{20}Fe_{10}$ crystalline phases. RSC Adv. **6**, 5367 (2016). https://doi.org/10.1039/C5RA21093C
24. Peña Rodríguez, V.A., Rojas-Ayala, C., Medina Medina, J., Paucar Cabrera, P., Quispe-Marcatoma, J., Landauro, C.V., Rojas Tapia, J., Baggio-Saitovitch, E.M., Passamani, E.C.: $Fe_{50}Ni_{50}$ synthesized by high energy ball milling: A systematic study using X-ray diffraction, EXAFS and Mössbauer methods. Mater. Charact. **149**, 249–254 (2019). https://doi.org/10.1016/j.matchar.2019.01.036
25. Lee, S., Edalati, K., Iwaoka, H., Horita, Z., Ohtsuki, T., Ohkochi, T., Kotsugi, M., Kojima, T., Mizuguchi, M.: and Koki Takanashi: Formation of FeNi with L10-ordered structure using high-pressure torsion. Philos. Mag. **94**(10), 639–646 (2014). https://doi.org/10.1080/09500839.2014.955546
26. BrukerAXS. DIFFRACPlus TOPAS: TOPAS 4.2 User Manual, Bruker-AXS GmbH,.Karlsruhe, Germany (2008)
27. Newville, M.: IFEFFIT: interactive XAFS analysis and FEFF fitting. J. Synchrotron Rad. **8**, 322–324 (2001). https://doi.org/10.1107/S0909049500016964
28. Ravel, B., Newville, M.: ATHENA, ARTEMIS, HEPHAESTUS: data analysis for X-ray absorption spectroscopy using IFEFFIT. J. Synchrotron Radiat. **12**(4), 537–541 (2005). https://doi.org/10.1107/S0909049505012719
29. Peña Rodríguez, V.A., Quispe Marcatoma, J., Rojas Ayala, Ch., Baggio-Saitovitch, E.M., Passamani, E.C.: Local environments of Fe and Co in $(Fe_{0.5}Co_{0.5})_{75}Si_{15}B_{10}$ mechanically alloyed. J. Alloys and Compd. **45**, 29–34 (2009). https://doi.org/10.1016/j.jallcom.2008.07.104

30. Zabinsky, S.I., Rehr, J.J., Ankudinov, A., Albers, R.C., Eller, M.J.: Multiple-scattering calculations of x-ray-absorption spectra. Phys. Rev. B **52**, 2995–3009 (1995). https://doi.org/10.1103/PhysRevB.52.2995
31. Ankudinov, A.L., Ravel, B., Rehr, J.J., Conradson, S.D.: Real-space multiple-scattering calculation and interpretation of x-ray-absorption near-edge structure. Phys. Rev. B **58**, 7565–7576 (1998). https://doi.org/10.1103/PhysRevB.58.7565
32. Müller, J.E., Jepsen, O., Wilkins, J.W.: X-ray absorption spectra: K-edge of 3d transition metals, L-edges of 3d and 4d metals and M-edges of palladium. Solid State Commun. **42**(5), 365–368 (1982). https://doi.org/10.1016/0038-1098(82)90154-5
33 Benitez Rodríguez, E.D., Rodríguez, H.B., Oyola Lozano, D., Rojas Martínez, Y.A., Pérez Alcázar, G.A.: Mössbauer study of alloy $Fe_{67.5}Ni_{32.5}$, prepared by mechanical alloying. Hyperfine Interact. **232**, 87–95 (2015). https://doi.org/10.1007/s10751-015-1138-8
34 Suryanarayana, C., Sharma, S.: Lattice contraction during amorphization by mechanical alloying. J. Appl. Phys. **104**, 103503 (2008). https://doi.org/10.1063/1.3020531
35. Hong, L.B., Fultz, B.: Two-phase coexistence in Fe–Ni alloys synthesized by ball milling. J. Appl. Phys. **79**, 3946–3955 (1996). https://doi.org/10.1063/1.361821
36. Lima, E., Drago, V.: Influence of chemical disorder on the magnetic behaviour and phase diagram of the Fe_xNi_{1-x} system. J. Magn. Magn. Mater. **280**, 251–256 (2004). https://doi.org/10.1016/j.jmmm.2004.03.020
37. Zhang, F.X., Jin, K., Zhao, S., Mu, S., Bei, H., Liu, J.C., Xue, H.Z., Popov, D., Park, C., Stocks, G.M., Weber, W.J., Zhang, Y.: X-ray absorption investigation of local structural disorder in Ni_{1-x} Fe_x (x=0.10, 0.20, 0.35, and 0.50) alloys. J. Appl. Phys. **121**, 165105 (2017). https://doi.org/10.1063/1.4982705
38. Clarke, R.S., Jr., Scott, E.R.D.: Tetrataenite-ordered FeNi, a new mineral in meteorite. Am. Mineral. **65**(7–8), 624–630 (1980)
39. Abdu, Y.A., Ericsson, T., Annersten, H., Dubrovinskaia, N.A., Dubrovinsky, L.S., Gimselseed, A.M.: Mössbauer studies on the metallic phases of Al Kidirate and New Haifa meteorites. Hyperfine Interact. (C) **5**, 375–378 (2002). https://doi.org/10.1007/978-94-010-0281-3_93
40. Scorzelli, R.B., Danon, J.: Mössbauer Spectroscopy andX-Ray Diffraction Studies of Fe-Ni Order-Disorder Processes in a 35% Ni Meteorite (Santa Catharina). Phys. Scr. **32**(2), 143–148 (1985). https://doi.org/10.1088/0031-8949/32/2/010
41. Lima, E., Jr., Drago, V.: A New Process to Produce Ordered $Fe_{50}Ni_{50}$ Tetrataenite. Phys. Stat. Sol. (a) **187**(1), 119–124 (2001). https://doi.org/10.1002/1521-396X(200109)187:1%3c119::AID-PSSA119%3e3.0.CO;2-L
42. Albertsen, J.F., Roy-Poulsen, N.O., Vistisen, L.: Ordered FeNi, Tetrataenite, and the Cooling Rate of Iron Meteorites Below 320 °C. Meteoritics **15**, 258 (1980)
43 González, J.M., Pérez Alcazar, G.A., Zamora, L.E., Tabares, J.A., Bohórquez, A., Gancedo, J.R.: Development of magnetic softness in high-energy ball milling alloyed $Fe_{50}B_{50}$. J. Magn. Magn. Mater. **261**, 337–346 (2003). https://doi.org/10.1016/S0304-8853(02)01321-5